

1 **Accepted**

2 **High-pressure phase behavior and equations of state of ThO₂ polymorphs**

3 **Authors:** Bethany A. Chidester^{1,*†}, Olivia S. Pardo^{1,††}, Rebecca A. Fischer^{1,†††}, Elizabeth
4 C. Thompson¹, Dion L. Heinz¹, Clemens Prescher^{2,††††}, Vitali B. Prakapenka², and
5 Andrew J. Campbell¹

6 **Affiliations:** ¹Department of the Geophysical Sciences, University of Chicago, Chicago,
7 IL 60637

8 ²GeoSoilEnviroCARS, University of Chicago, Argonne National Laboratory, Argonne,
9 IL 60439

10 [†]Present address: Earth and Planetary Sciences Department, University of California
11 Davis, Davis, CA 95616

12 ^{††}Present address: Division of Geological and Planetary Sciences, California Institute of
13 Technology, Pasadena, CA 91125

14 ^{†††}Present address: Department of Earth and Planetary Sciences, Harvard University,
15 Cambridge, MA 02138

16 ^{††††}Present address: Institut für Geologie und Mineralogie, Universität zu Köln, 50674
17 Köln, Germany

18 *Email: bchides@sandia.gov

19

20 *Submitted to American Mineralogist, June 13, 2017.*

21 *Revised and resubmitted to American Mineralogist, November 16, 2017*

22 *Accepted on January 30, 2018*

23

24 **ABSTRACT**

25 ThO₂ is an important material for understanding the heat budget of Earth's mantle, as
26 well as the stability of nuclear fuels at extreme conditions. We measured the in situ high-
27 pressure, high-temperature phase behavior of ThO₂ to ~60 GPa and ~2500 K. It
28 undergoes a transition from the cubic fluorite-type structure (thorianite) to the
29 orthorhombic α -PbCl₂ cotunnite-type structure between 20 and 30 GPa at room
30 temperature. Prior to the transition at room temperature, an increase in unit cell volume is
31 observed, which we interpret as anion sub-lattice disorder or pre-transformation
32 "melting" (Bouffefel et al., 2006). The thermal equation of state parameters for both
33 thorianite ($V_0 = 26.379(7)$, $K_0 = 204(2)$, $\alpha K_T = 0.0035(3)$) and the high-pressure cotunnite-
34 type phase ($V_0 = 24.75(6)$, $K_0 = 190(3)$, $\alpha K_T = 0.0037(4)$) are reported, holding K_0 fixed
35 at 4. The similarity of these parameters suggests that the two phases behave similarly
36 within the deep Earth. The lattice parameter ratios for the cotunnite-type phase change
37 significantly with pressure, suggesting a different structure is stable at higher pressure.

38

39 **INTRODUCTION**

40 Actinides, specifically U and Th, are important in the Earth as long-lived
41 radioactive heat producing elements. Assuming the refractory lithophile element budget
42 of the bulk silicate Earth is chondritic in composition, these elements produce up to 36%
43 of the total heat fluxed out of the planet's surface, but their distribution and role within
44 the dynamics of the deepest part of Earth's mantle is unknown (McDonough and Sun,
45 1995). These elements are highly refractory (ThO₂ has the highest melting temperature of
46 any oxide at ambient pressures at 3663 K) and nominally incompatible in major mantle

47 minerals, meaning they tend to partition into melts or accessory phases, which makes
48 them excellent tracers for chemical reservoirs in the deep Earth as well as within other
49 planetary bodies (Arevalo Jr. et al., 2009; Fonseca et al., 2014). Additionally, U and Th
50 and their oxides are increasingly important as nuclear energy sources for our growing
51 population and they are used in thermally resistant ceramics (Cuney, 2013). However,
52 stable materials that resist decomposition or amorphization under varying pressure,
53 temperature, and radiation conditions are needed to contain and immobilize the resulting
54 waste from this industrial usage. Actinide-bearing minerals that are stable under a variety
55 of thermodynamic conditions can point to analogous materials that are stable at ambient
56 conditions. Thus, exploring the mineralogy of actinide-bearing minerals at the extreme
57 pressure and temperature conditions of Earth's mantle (tens of gigapascals and thousands
58 of Kelvin) is universally important. This paper focuses on the high-pressure, high-
59 temperature phase behavior and equations of state of the simplest Th-bearing mineral,
60 ThO₂.

61 End-member ThO₂ (thorianite) takes the cubic fluorite-type (CaF₂, *Fm3m*)
62 structure at ambient conditions (Fig. 1a). Room temperature X-ray diffraction (XRD)
63 studies show that upon compression this material undergoes a reconstructive phase
64 transition to the orthorhombic cotunnite-type structure (α -PbCl₂, *Pnma*) (Fig. 1b)
65 (Dancausse et al., 1990; Idiri et al., 2004; Jayaraman et al., 1988; Olsen et al., 2004). This
66 phase transition results in an increase in coordination number of the Th cation, from 8-
67 fold (cubic) in the fluorite-type structure to 9-fold in the cotunnite-type structure. At
68 room temperature, this phase transition is kinetically inhibited, with the high-pressure
69 phase first appearing between 30-40 GPa, and coexisting with the metastable low-

70 pressure phase until 55-57 GPa when the transition is observed to be complete. Because
71 of this sluggishness, the precise position of the equilibrium phase boundary is not well
72 constrained.

73 Materials in the fluorite-type structure, including ThO₂, have been shown to
74 undergo a “superionic” transition at about 80% the melting temperature of the material,
75 whereby a critical concentration of Frenkel defects occur in the crystal, resulting in anion
76 sub-lattice “melting” (Clausen et al., 1989; Kuksin and Smirnova, 2014; Kupryazhkin et
77 al., 2011; March et al., 1980; Matveev and Veshchunov, 1997). This transition includes
78 an exponential increase in the enthalpy and specific heat of the material. One
79 computational study has suggested that this transition also occurs at ambient temperature
80 under increasing pressure in the type specimen of fluorite, CaF₂ (Boufelfel et al., 2006).
81 In this case, the formation of a Frenkel defect, in which a F⁻ anion shifts from its
82 tetrahedral site to a previously empty octahedral site, allowing another F⁻ anion to take its
83 place, locally expands the lattice and allows the Ca cations to subsequently shift to their
84 new crystallographic position in the cotunnite-type structure at high pressures.

85 Previous experiments have shown that phase transitions in similar systems, such
86 as some of the rare Earth pyrochlore (A₂Zr₂O₇)/defect-fluorite ((A,Zr)₄O₇) zirconate
87 materials, which often undergo either amorphization or structural transition to the (defect)
88 cotunnite-type structure under pressure, exhibit anomalous volume expansion just prior to
89 the phase transition (Rittman et al., 2017; Zhang et al., 2010). However, this volume
90 expansion has not been recognized universally in other pyrochlore systems (Li et al.,
91 2016; Rittman et al., 2017). It is likely that the anions in these more complicated
92 pyrochlore compounds are undergoing a similar distortion to the one described above for

93 CaF₂, although it may be dependent upon the relative radii of the cations in the A and B
94 sites (Rittman et al., 2017). A recent Raman spectroscopy study on bulk ThO₂ under
95 pressure has suggested that this material also experiences anion sub-lattice disorder at
96 high pressures (Kamali et al., 2017). It was recognized in that study that one Raman
97 mode appeared within the ThO₂ spectrum at ~25 GPa as shoulder on the F_{2g} mode of
98 fluorite-type ThO₂, approximately 10 GPa lower than the rest of the cotunnite-type
99 modes appeared in the spectrum (~37 GPa). This mode is thought to signal anion disorder
100 since the F_{2g} mode results from the breathing of O anions around the Th cation, thus it is
101 only sensitive to movements of the O atoms. UO₂ also exhibits shoulders on the F_{2g} peak,
102 which are thought to be related to anion sub-lattice disorder, but in this case the disorder
103 may be enhanced due to a slight excess of O in the structure (hyperstoichiometry)
104 (Crowhurst et al., 2015).

105 The thermo-elastic parameters (e.g. bulk modulus, K , and thermal expansion, α)
106 of this material are necessary for describing its thermodynamic behavior at extreme
107 conditions of pressure and temperature. Recent measurements (XRD, ultrasonic) and
108 calculations of the ambient-pressure isothermal bulk modulus (K_0) of pure thorianite at
109 300 K are consistent around 185-198 GPa with a pressure derivative ($dK/dP = K_0'$, where
110 relevant) of ~5 (Boettger, 2009; Boudjemline et al., 2011; Idiri et al., 2004; Kanchana et
111 al., 2006; Li et al., 2014; Macedo et al., 1964; Olsen et al., 2004; Shein et al., 2007; Wang
112 et al., 2010). Earlier XRD studies resulted in much higher values of K_0 and K_0' - 262 GPa
113 and 6.7, respectively (Dancausse et al., 1990), while an inelastic X-ray scattering
114 experiment and a different series of calculations predicted K_0 values around 220 GPa
115 (Clausen et al., 1989; Kanchana et al., 2006; Li et al., 2002; Olsen et al., 2004; Sevik and

116 Çağın, 2009). These results are summarized in Table 1. To date, no experimental studies
117 have reported on the behavior of this material at simultaneous high pressures and high
118 temperatures or on the equation of state of the high-pressure cotunnite-type phase.
119 Calculations of the elastic parameters of the high-pressure phase are inconsistent, ranging
120 in values between $K_0 = 148\text{-}207$ and $K_0' = 4.2\text{-}7.8$ (Boettger, 2009; Boudjemline et al.,
121 2011; Li et al., 2014; Wang et al., 2010). In this study, we conducted in situ XRD
122 measurements of ThO₂ to ~60 GPa and ~2500 K to more precisely define the thorianite–
123 cotunnite-type phase boundary and to measure the thermal equation of state parameters
124 for both the low- and high-pressure phases of this material.

125

126 **SYNCHROTRON X-RAY DIFFRACTION AND RAMAN SPECTROSCOPY**

127 **EXPERIMENTS**

128 Four synchrotron powder X-ray diffraction (XRD) experiments on ThO₂ were
129 conducted in the laser-heated diamond anvil cell (LH-DAC), with diamond culets of 300
130 μm or 250 μm. ThO₂ (99.99%) was purchased from Strem Chemical. The ThO₂ starting
131 material was characterized by an ambient condition XRD measurement at the University
132 of Chicago using incident radiation of $\lambda = 1.5418 \text{ \AA}$ (Cu K α) and Si powder (NBS 640a)
133 as an X-ray standard. In high P - T experiments, amorphous Pt (Alfa Aesar, 0.2-1.6 μm,
134 99.9%) was mixed with the ThO₂ as an absorber for laser heating. The ThO₂/Pt mixture
135 was loaded as a powder between flakes of KCl (reagent grade, Alfa Aesar) or KBr
136 (spectroscopy grade, Alfa Aesar), which acted as the pressure medium, thermal insulator
137 and pressure standard in the high-temperature experiments (Dewaele et al., 2012).
138 Sample B12 was measured at room temperature using cryogenically-loaded Ar as the

139 pressure medium and pressure standard (Ross et al., 1986). A 3% uncertainty was
140 assigned to the accuracy of the Ar pressure standard.

141 Following safety regulations for radiogenic samples at the Department of Energy
142 facilities where these measurements were made, experiments used double containment to
143 prevent accidental environmental contamination or dispersal. The gasket and diamonds
144 provided the first layer of containment. For the second layer of containment, the DACs
145 were securely wrapped in Kapton® tape around the diameter of the cell. In the laser-
146 heating path, thin (0.5 mm) sapphire windows (6.35 mm diameter, Edmund Optics) were
147 adhered to the outside of the diamond seat by epoxy. The sapphire windows typically
148 resulted in several large and distinctive X-ray diffraction spots on the detector, which
149 were masked during data analysis.

150 Room temperature angle-dispersive powder XRD experiments were performed at
151 sector 12.2.2 at the Advanced Light Source (ALS), Lawrence Berkeley National
152 Laboratory, using a monochromatic incident X-ray beam ($\lambda = 0.4959 \text{ \AA}$) of $\sim 10 \text{ \mu m}$ in
153 diameter. High-temperature XRD experiments were conducted at sector 13-ID-D (GSE-
154 CARS) of the Advanced Photon Source (APS), Argonne National Laboratory, using a
155 monochromatic incident X-ray ($\lambda = 0.3344 \text{ \AA}$) typically measuring $\sim 3 \times 4 \text{ \mu m}$. At both
156 facilities, sample to detector distance and tilt were calibrated using LaB₆. High-
157 temperature samples were compressed to a target pressure and laser heated while XRD
158 measurements were simultaneously collected. The heating laser was co-aligned with the
159 X-ray beam using the X-ray induced fluorescence of the KCl or KBr insulator. Laser-
160 heating was done from both sides of the sample, adjusting upstream and downstream
161 laser power to balance the temperature. Surface temperatures were measured spectro-

162 radiometrically using the Planck radiation function (Prakapenka et al., 2008), and
163 corrected by -3% to account for the axial temperature gradient across the sample
164 (Campbell et al., 2007). The temperature of the alkali halide thermal insulator was
165 estimated as the midpoint between the surface of the sample and the surface of the
166 diamond anvil as described by Campbell et al. (2009).

167 Powder XRD patterns were collected on a CCD and azimuthally integrated to
168 intensity vs. 2θ (degrees) plots using DIOPTAS (Prescher and Prakapenka, 2015). Lattice
169 parameters as a function of pressure and temperature were determined by fitting
170 reflection positions using PeakFit (Systat Software). At least one XRD pattern per
171 heating cycle was fully indexed to confirm the space group and lattice parameters at each
172 pressure step using GSAS-II (Toby and Von Dreele, 2013) or DICVOL04 (Boultif and
173 Louër, 2004), which is part of the FULLProf Suite (Rodriguez-Carvajal, 1993).

174 In addition to XRD measurements, the room-temperature phase behavior of ThO_2
175 was investigated using Raman spectroscopy in the Laboratory for Mineral Physics at the
176 University of Chicago. Samples were prepared either as ThO_2 powder pressed between
177 two MgO flakes, which acted as a Raman-inactive pressure-transmitting medium, or
178 without a pressure medium. All samples were loaded in a steel gasket with an $80\ \mu\text{m}$
179 sample chamber and $300\ \mu\text{m}$ culet DAC. Measurements were taken using a 0.75-meter
180 Acton SpectraPro monochromator with a 473 nm 150 mW blue laser. Pressure was
181 determined using the Raman shift of the diamond, which was calibrated to ruby under
182 quasi-hydrostatic conditions after Akahama and Kawamura (2007). Raman acquisitions
183 were centered at $712\ \text{cm}^{-1}$ to minimize nearby diamond Raman interference and were the
184 average of 600 one-second exposures at full laser power. Compression measurements

185 began at 3-5 GPa and samples were incrementally brought to ~60 GPa before
186 decompressing to ambient pressure. Raman mode frequencies were determined by peak
187 fitting using PeakFit (Systat Software). The reported frequencies are an average of three
188 individual fits and the reported uncertainty is the corresponding standard deviation.

189

190 **RESULTS AND DISCUSSION**

191 **Phase diagram ThO₂**

192 The measured lattice parameters and pressure-volume-temperature (*P-V-T*) data
193 points from the in situ XRD experiments are listed in Supplemental Table 1 (thorianite)
194 and Supplemental Table 2 (cotunnite-type ThO₂). Ambient pressure XRD measurement
195 of the ThO₂ starting material confirmed an initial fluorite-type structure (Fig. 1a) with a
196 lattice parameter of $a = 5.5958 \pm 0.0005 \text{ \AA}$ ($V_0 = 26.379 \pm 0.007 \text{ cm}^3/\text{mole}$), consistent
197 with literature values for end-member thorianite (Table 1). As with previous studies,
198 synchrotron XRD measurements at high pressure and room temperature demonstrate that
199 thorianite exists in this fluorite-type structure until ~34 GPa, at which point new
200 diffraction peaks appear between the (111) and (200) fluorite peaks, indicating the
201 emergence of the cotunnite-type phase, illustrated in Fig. 1b (Dancausse et al., 1990; Idiri
202 et al., 2004; Jayaraman et al., 1988; Olsen et al., 2004). Figure 2 shows high-temperature
203 examples of raw diffraction images and their corresponding integrated spectra (intensity
204 vs. 2θ) for this phase transition, as well as a higher *P-T* pattern containing only the
205 cotunnite-type phase.

206 The fluorite–cotunnite phase transition requires a crystallographic reconstruction,
207 which is characterized by a large degree of kinetic inhibition. As with previous XRD

208 measurements at room temperature, the fluorite-type phase was present up to the highest
209 pressures achieved at room temperature in this study, ~54 GPa (Dancausse et al., 1990;
210 Idiri et al., 2004; Olsen et al., 2004). This kinetic barrier has been previously observed in
211 room temperature compression studies using different techniques. Using Raman
212 spectroscopy, Jayaraman et al. (1988) observed the initiation of the phase transition
213 between 30 and 37 GPa, but did not reach high enough pressures to observe the
214 disappearance of the fluorite-type phase. The slight differences in the observed transition
215 pressure range in these studies (i.e. 54-57 GPa) are likely due to the use of different
216 pressure-transmitting media. Klotz et al. (2009) have measured the hydrostatic limits, as
217 well as the standard deviation from true pressure (calibrated to ruby) across the sample
218 chamber over a wide range of pressures for all of the pressure media used in the studies
219 described here. Our study used Ar as the room-temperature pressure medium, which is
220 more hydrostatic (i.e. exhibits a lower standard deviation from true pressure) at these
221 pressures and allows for a greater range of metastability than the pressure media in
222 previous studies, silicone oil, N₂, or 16:3:1 methanol:ethanol:water (Dancausse et al.,
223 1990; Idiri et al., 2004; Klotz et al., 2009; Olsen et al., 2004). The less hydrostatic
224 conditions in these studies created higher strains, resulting in more abrupt phase
225 transitions compared to the more hydrostatic conditions reported here.

226 In the room temperature volume vs. pressure (*V-P*) XRD data from this study and
227 those from the literature (Fig. 3), a discontinuity in compression behavior is observed
228 around ~16 GPa, similar to the discontinuities observed previously in other fluorite-type
229 and pyrochlore materials at high pressures (Rittman et al., 2017; Zhang et al., 2010).
230 Although the crystal structure remains in the fluorite-type phase above this pressure, the

231 measured volume is greater than expected by normal compressibility. We interpret this as
232 evidence of anion sub-lattice disorder in ThO₂ (Boulfelfel et al., 2006).

233 As described in the Introduction, during the fluorite–cotunnite transition the
234 anions are subject to local disordering, described by Boulfelfel et al. (2006) as “melting”
235 of the anionic sub-lattice. This effectively increases the local volume, and allows the
236 cations to subsequently rearrange. Thus, the change in compressibility is interpreted as
237 the onset of the fluorite–cotunnite phase transition. Our data show this discontinuity
238 much more intensely than the earlier literature data for ThO₂ (Idiri et al., 2004; Olsen et
239 al., 2004), which again is likely due to the differences in deviatoric stress conditions of
240 the measurements (Klotz et al., 2009). It is unclear whether this process is also evident in
241 the room temperature compression curve for the cotunnite-type phase because the room
242 temperature XRD patterns that contained that phase were not well enough resolved to
243 extract lattice parameters or volumes.

244 To further investigate this phase transition process, we performed Raman
245 spectroscopy at room temperature under non-hydrostatic conditions. As described in the
246 Methods section, measurements were made both on compression and decompression.
247 Examples of the compression spectra are shown in Fig. 4. Under these conditions,
248 thorianite exhibits a single (triply degenerate) Raman absorption mode representing the
249 symmetric breathing of the O anions around the Th cation (F_{2g}) at $\sim 474\text{ cm}^{-1}$ at 5 GPa.
250 This peak broadens and shifts to higher wavenumbers with increasing pressure throughout
251 the pressure range investigated. At ~ 22 GPa new peaks appear as a shoulder or very near
252 the F_{2g} peak at 540 (M1) and 622 (M2) cm^{-1} . Above 32 GPa a triplet of absorption modes
253 (M3-M5) become apparent at low wavenumbers, 330-390 cm^{-1} and a single peak

254 becomes resolvable at 495 cm^{-1} (M6). One final peak at $\sim 330\text{ cm}^{-1}$ (M8) is resolved
255 above 50 GPa (Figs. 4 and 5). Group theory indicates that the cotunnite-type structure
256 should result in 18 distinct Raman modes. We observe 8 at the highest pressures reached.
257 Although our spectra are rather broad due to pressure effects, they are very similar to
258 those observed at ambient pressures in samples of cotunnite-type ZrO_2 and HfO_2
259 recovered from high pressures (Haines et al., 1997). The pressure dependence of these
260 high-pressure absorption frequencies is shown in Fig. 5 and tabulated, along with
261 calculated mode Grüneisen parameters in Table 2. Mode Grüneisen parameters describe
262 the volume dependence of the frequency of each individual vibrational mode. The
263 thermodynamic Grüneisen parameter is a weighted mean of all mode Grüneisen
264 parameters for the material, including the acoustic modes and other Raman-inactive
265 modes which were not probed in this study.

266 We interpret the additional peaks in the 20-30 GPa range as the rearrangement of
267 the anion sub-lattice, which is consistent with previous interpretations of Raman
268 measurements of ThO_2 (Kamali et al., 2017), although these limited data cannot be used
269 to determine the extent of disorder. The peaks appearing at 32 GPa are the final stages of
270 the fluorite–cotunnite phase transition. The vibrational modes exhibit a regular linear
271 slope as a function of pressure above 37 GPa. Thus, the full crystallographic
272 reconstruction of the cubic fluorite-type structure to the orthorhombic cotunnite-type
273 structure appears to be complete for both the anions and cations between 32 and 37 GPa.
274 This is approximately the pressure at which the cotunnite phase emerges in the room
275 temperature XRD data (Fig. 6) (Dancausse et al., 1990; Idiri et al., 2004; Olsen et al.,
276 2004). Since XRD is more sensitive to the Th atoms in this material, it appears that the

277 phase transition will not be evident using diffraction until a significant portion of the
278 cation sub-lattice has undergone transformation (i.e. above 32 GPa). Given the change in
279 slope of the Raman frequencies, none of the high-pressure modes appear to be directly
280 related to the low-pressure phase. Upon decompression, the cotunnite-type absorption
281 peaks remain until ~ 2 GPa while continually decreasing in Raman frequency. At ~ 1 GPa,
282 there is only a single peak remaining, at 463 cm^{-1} , suggesting that it has fully reverted
283 back to the fluorite-type structure.

284 The thorianite–cotunnite-type phase transition is also observed at high
285 temperatures. In synchrotron XRD experiments at ~ 17 GPa, the phase transition occurred
286 on increasing temperature between 1534 ± 114 K and 1583 ± 119 K. Again, this
287 transition is sluggish, even at high temperatures. The high-pressure phase was not
288 observed at all in the pressure step at ~ 18 - 19 GPa, which suggests that in those cases
289 heating was faster than the phase transition could proceed. Additionally, from 20 - 30 GPa
290 at high temperatures both phases are observed, but only one of them (likely the cotunnite-
291 type phase) can be thermodynamically stable. Above ~ 30 GPa at high temperatures, only
292 the cotunnite-type phase is observed up to the highest pressures reached in this study, ~ 62
293 GPa. All of this information was compiled as our preferred P - T phase diagram for this
294 material in Fig. 6. Based on our observations, it is likely that the phase boundary is very
295 close to vertical or slightly negative around 18 - 20 GPa in P - T space, although it is not
296 observed in the XRD data until ≥ 30 GPa.

297

298 **Equations of state of ThO₂ polymorphs**

299 Given the range of P - V - T data obtained for the polymorphs of ThO_2 in this study,
300 we were able to extract equation of state parameters for each phase. We fit both sets of
301 data to the Mie-Grüneisen type equations of state (eq. 1), where the reference pressure
302 (300 K) equation took the Birch-Murnaghan form (eq. 2).

$$303 \quad P = P_{300K} + P_{thermal} \quad (1)$$

$$304 \quad P_{300K} = 3K_0 f(1 + 2f)^{\frac{5}{2}} \left(1 + \frac{3}{2} f(K_0' - 4) \right) \quad (2)$$

305 Here, f is the finite Eulerian strain, $\frac{1}{2} \left(\left(\frac{V}{V_0} \right)^{\frac{-2}{3}} - 1 \right)$, V is the measured volume of the
306 material at pressure, P , V_0 is the ambient pressure volume, K_0 is the ambient pressure
307 isothermal bulk modulus, and K_0' is its pressure derivative. For the thorianite equation of
308 state, we only used the room temperature data prior to the volume discontinuity (<15
309 GPa). For the cotunnite-type phase, there were no room temperature patterns of high
310 enough quality to extract lattice parameters. Thus, no room temperature data were used in
311 the fits for the high-pressure phase. Because of the limited room temperature data, we
312 chose to define the thermal pressure as in equation 3.

$$313 \quad P_{thermal} = \alpha K_T (T - 300) \quad (3)$$

314 α is thermal expansion and K_T is the bulk modulus at temperature, T . In this case, the
315 coefficient on temperature is taken to be constant.

316 The equation of state parameters for each phase are given in Table 1, along with
317 the available literature values. For thorianite, V_0 was measured prior to the compression
318 experiments to be 26.379(7) cm^3/mole , so it was fixed in the fitting routine. Additionally,
319 K_0' was fixed to a value of 4 to allow for more precise determination of the thermal term.
320 Our choice of 4 of K_0' is slightly lower than has previously been measured (~5), so our

321 measured bulk modulus is slightly higher at 204 GPa than other recent XRD studies (Idiri
322 et al., 2004; Olsen et al., 2004). The thermal pressure coefficient, αK_T , for thorianite was
323 determined to be 0.0035(3) GPa/K.

324 The properties of the high-pressure cotunnite-type phase of ThO₂ are very similar
325 to those of the low-pressure phase. Holding K_0' at a value of 4, the bulk modulus for this
326 phase was determined to be 190(3) GPa. This is slightly more compressible, but very
327 similar to the value for thorianite. Additionally, the thermal pressure coefficient was
328 found to be 0.0037(4) GPa/K, suggesting that the high-pressure phase reacts very
329 similarly to pressure and temperature as the low-pressure phase. The fitted zero-pressure
330 volume for the cotunnite-type phase is 24.75(6) cm³/mole, which is 6.2% more dense
331 than thorianite at ambient conditions. This is virtually the same volume contrast that was
332 observed at ~35 GPa, by Idiri et al. (2004). The compiled P - V - T data from this study are
333 plotted in Fig. 7 along with calculated isotherms for comparison.

334 The values for the individual lattice parameters of the cotunnite-type phase are
335 given in the top panel of Fig. 8. Each one decreases with pressure, as expected, but the a -
336 axis appears to be compressing at a faster rate than either b or c , while the short b -axis
337 changes very little. This relationship is best demonstrated in the lattice parameter ratios as
338 a function of pressure in the lower panels of Fig. 8. In general, the ratios of the lattice
339 parameters change linearly with pressure, with only small dependencies on temperature.
340 This would occur if the coordination polyhedra within the cotunnite-type structure are
341 continuously distorting with pressure, and suggests that upon increasing compression the
342 material will undergo another structural phase transition. A transition of this type has
343 been predicted theoretically for ThO₂ above ~80 GPa by Perry et al. (2017). In the

344 calculation, the phase transition was signaled by a collapse in the a -axis and a
345 corresponding expansion of the b - and c -axes, which is consistent with the compression
346 behavior observed here. Some likely options for this higher pressure phase are common
347 post-cotunnite structures, including the hexagonal Fe_2P structure ($P\bar{6}2m$) observed in the
348 ZrO_2 system (Nishio-Hamane et al., 2015) or the Ni_2In structure ($P6_3/mmc$) and
349 orthorhombic distortions thereof (Song et al., 2012). For convenience, the ratios have
350 been fitted to a linear dependence of pressure. The slopes and hypothetical zero-pressure
351 values from these fits are given in Table 3.

352

353 **IMPLICATIONS**

354 This study explores the simultaneous high-pressure, high-temperature behavior of
355 ThO_2 . We find that the thorianite–cotunnite-type phase transition is kinetically inhibited,
356 even at 2000 K. The onset of the transition at room temperature begins at ~15-20 GPa, as
357 evidenced by an anomalously low compressibility of the cubic structure with pressure.
358 We interpret this change as anion sub-lattice disorder, which has been theoretically
359 predicted for the same phase transition in CaF_2 (Boufelfel et al., 2006) and observed in
360 several analogous phase transitions in the pyrochlore/disordered fluorite system under
361 pressure (Rittman et al., 2017; Zhang et al., 2010). This transition pressure is
362 corroborated by Raman spectroscopy measurements (Figs. 4 and 5) (Jayaraman et al.,
363 1988; Kamali et al., 2017). At room temperature, the phase transition was not complete,
364 even at the highest pressures reached in this study, ~55 GPa. At high temperatures, the
365 onset of the phase transition was observed at ~18 GPa and was complete by ~30 GPa. If
366 Th exists in oxide form in the Earth's lower mantle, it is likely in a solid solution with

367 other large cations of +4 valence whose oxides also take the cotunnite structure, e.g.
368 (Zr,Th,U)O₂. Such a phase, with Zr as the dominant (i.e. most abundant) cation, could
369 exist in the cotunnite-type structure to at least ~1430 km (~60 GPa), as ZrO₂ has been
370 shown to be stable in the cotunnite-type structure well above this pressure (Nishio-
371 Hamane et al., 2015).

372 The isothermal equation of state parameters measured here for thorianite are
373 consistent with previous measurements (Idiri et al., 2004; Olsen et al., 2004).
374 Additionally, this study provides a thermal dependence for the high-pressure behavior of
375 thorianite, as well as thermal equation of state parameters for the high-pressure cotunnite-
376 type phase. These parameters are necessary for predicting the behavior of this material at
377 extreme conditions, such as within a nuclear reactor (a very high radiation environment at
378 ~15 MPa and several hundred Celsius for pressurized water reactors (Office of Nuclear
379 Reactor Regulation, 2012)) or in the Earth's lower mantle (up to 137 GPa and ~4000 K at
380 the core-mantle boundary). We find that, although the cotunnite-type phase of ThO₂ is
381 ~6% denser than its lower-pressure polymorph, they have a very similar compressibilities
382 and thermal pressure coefficients. We also find that the cotunnite structure is
383 continuously deforming under pressure, which suggests that this material will undergo
384 another phase transition on increasing pressure. Such a phase transition has been
385 predicted above ~80 GPa theoretically (Perry et al., 2017). Thus, actinide-bearing oxides
386 in the lowermost region of Earth's lower mantle may not be stable in the cotunnite-type
387 phase. This behavior has the potential to influence the distribution of large ion lithophile
388 elements among accessory phases, particularly if the post-cotunnite structure exhibits a
389 significantly different coordination environment than the cotunnite-type structure.

390

391 **ACKNOWLEDGMENTS**

392 The authors are grateful to Jinyuan Yan for his assistance with the room temperature
393 measurements. This study was funded by NSF Graduate Research Fellowship Grant
394 #DGE-1144082, NSF Grants #EAR-1427123 and #EAR-0944298, and the
395 Carnegie/DOE Alliance Center (CDAC). Portions of this work were done at
396 GeoSoilEnviroCARS (The University of Chicago, Sector 13) of the Advanced Photon
397 Source, Argonne National Laboratory, and at Sector 12.2.2 of the Advanced Light
398 Source, Lawrence Berkeley National Laboratory. GeoSoilEnviroCARS is supported by
399 the National Science Foundation - Earth Sciences (EAR - 1634415) and Department of
400 Energy- GeoSciences (DE-FG02-94ER14466). This research used resources of the
401 Advanced Photon Source, a U.S. Department of Energy (DOE) Office of Science User
402 Facility operated for the DOE Office of Science by Argonne National Laboratory under
403 Contract No. DE-AC02-06CH11357. Sector 12.2.2. is funded in part by the Consortium
404 for Materials Properties Research in Earth Sciences (COMPRES) under NSF Cooperative
405 Agreement EAR 10-43050. The Advanced Light Source is supported by the Director,
406 Office of Science, Office of Basic Energy Sciences, of the U.S. Department of Energy
407 under Contract No. DE-AC02-05CH11231.

408

409

410 **REFERENCES**

411
412 Akahama, Y., and Kawamura, H. (2007) Diamond anvil Raman gauge in multimegabar
413 pressure range. *High Pressure Research*, 27(4), 473-482.

414 Arevalo Jr., R., McDonough, W.F., and Luong, M. (2009) The K/U ratio of the silicate
415 Earth: Insights into mantle composition, structure and thermal evolution. *Earth
416 and Planetary Science Letters*, 278, 361-369.

417 Boettger, J.C. (2009) Theoretical zero-temperature isotherm and structural phase stability
418 of thorium dioxide. *International Journal of Quantum Chemistry*, 109(15), 3564-
419 3569.

420 Boudjemline, A., Louail, L., Islam, M.M., and Diawara, B. (2011) Dependence of
421 pressure on elastic, electronic and optical properties of CeO₂ and ThO₂: A first
422 principles study. *Computational Materials Science*, 50(7), 2280-2286.

423 Boulfelfel, S.E., Zahn, D., Hochrein, O., Grin, Y., and Leoni, S. (2006) Low-dimensional
424 sublattice melting by pressure: Superionic conduction in the phase interfaces of
425 the fluorite-to-cotunnite transition of CaF₂. *Physical Review B*, 74(9), 094106.

426 Boultif, A., and Louër, D. (2004) Powder pattern indexing with the dichotomy method.
427 *Journal of Applied Crystallography*, 37, 724-731.

428 Campbell, A.J., Danielson, L., Righter, K., Seagle, C.T., Wang, Y., and Prakapenka, V.B.
429 (2009) High pressure effects on the iron–iron oxide and nickel–nickel oxide
430 oxygen fugacity buffers. *Earth and Planetary Science Letters*, 286(3-4), 556-564.

431 Campbell, A.J., Seagle, C.T., Heinz, D.L., Shen, G., and Prakapenka, V.B. (2007) Partial
432 melting in the iron–sulfur system at high pressure: A synchrotron X-ray
433 diffraction study. *Physics of the Earth and Planetary Interiors*, 162(1-2), 119-128.

434 Clausen, K.N., Hackett, M.A., Hayes, W., Hull, S., Hutchings, M.T., MacDonald, J.E.,
435 McEwen, K.A., Osborn, R., and Steigenberger, U. (1989) Coherent Diffuse
436 Neutron Scattering From UO₂ and ThO₂ at Temperatures Above 2000 K. *Physica
437 B*, 156-157, 103-106.

438 Crowhurst, J.C., Jeffries, J.R., Aberg, D., Zaug, J.M., Dai, Z.R., Siekhaus, W.J., Teslich,
439 N.E., Holliday, K.S., Knight, K.B., Nelson, A.J., and Hutcheon, I.D. (2015) A
440 combined theoretical and experimental investigation of uranium dioxide under
441 high static pressure. *Journal of Physics: Condensed Matter*, 27(26), 265401.

442 Cuney, M. (2013) Uranium and thorium resources and the sustainability of nuclear
443 energy. In P.C. Burns, and G.E. Sigmon, Eds. *Uranium: Cradle to Grave*,

444 Mineralogical Association of Canada Short Course Series, 43, p. 417-437.
445 Mineralogical Association of Canada.

446 Dancausse, J.-P., Gering, E., Heathman, S., and Benedict, U. (1990) Pressure-induced
447 phase transition in ThO₂ and PuO₂. *High Pressure Research*, 2(5-6), 381-389.

448 Dewaele, A., Belonoshko, A.B., Garbarino, G., Occelli, F., Bouvier, P., Hanfland, M.,
449 and Mezouar, M. (2012) High-pressure–high-temperature equation of state of KCl
450 and KBr. *Physical Review B*, 85(21), 214105.

451 Dorfman, S.M., Jiang, F., Mao, Z., Kubo, A., Meng, Y., Prakapenka, V.B., and Duffy,
452 T.S. (2010) Phase transitions and equations of state of alkaline earth
453 fluorides CaF₂, SrF₂, and BaF₂ to Mbar pressures. *Physical Review B*, 81(17).

454 Fonseca, R.O.C., Mallmann, G., Sprung, P., Sommer, J.E., Heuser, A., Speelmanns, I.M.,
455 and Blanchard, H. (2014) Redox controls on tungsten and uranium crystal/silicate
456 melt partitioning and implications for the U/W and Th/W ratio of the lunar
457 mantle. *Earth and Planetary Science Letters*, 404, 1-13.

458 Haines, J., Léger, J.M., Hull, S., Petitet, J.P., Pereira, A.S., Perottoni, C.A., and da
459 Jornada, J.A.H. (1997) Characterization of the cotunnite-type phases of zirconia
460 and hafnia by neutron diffraction and Raman spectroscopy. *Journal of the*
461 *American Ceramic Society*, 80(7), 1910-1914.

462 Idiri, M., Le Bihan, T., Heathman, S., and Rebizant, J. (2004) Behavior of actinide
463 dioxides under pressure: UO₂ and ThO₂. *Physical Review B*, 70(1), 014113.

464 Jayaraman, A., Kourouklis, G.A., and Van Uitert, L.G. (1988) A high pressure Raman
465 study of ThO₂ to 40 GPa and pressure-induced phase transition from fluorite
466 structure. *Pramana - Journal of Physics*, 30(3), 22-231.

467 Kamali, K., Ananthasivan, K., Ravindran, T.R., and Kumar, D.S. (2017) High pressure
468 Raman spectroscopic studies on nanocrystalline ThO₂. *Journal of Nuclear*
469 *Materials*, 493, 77-83.

470 Kanchana, V., Vaitheeswaran, G., Svane, A., and Delin, A. (2006) First-principles study
471 of elastic properties of CeO₂, ThO₂ and PoO₂. *Journal of Physics: Condensed*
472 *Matter*, 18(42), 9615-9624.

473 Klotz, S., Chervin, J.C., Munsch, P., and Le Marchand, G. (2009) Hydrostatic limits of
474 11 pressure transmitting media. *Journal of Physics D: Applied Physics*, 42(7),
475 075413.

476 Kuksin, A.Y., and Smirnova, D.E. (2014) Calculation of diffusion coefficients of defects
477 and ions in UO₂. *Physics of the Solid State*, 56(6), 1214-1223.

478 Kupryazhkin, A.Y., Svetlichnyi, D.G., and Zhiganov, A.N. (2011) Self-diffusion of
479 oxygen in superstoichiometric uranium dioxide in the range of the superionic
480 phase transition. *Technical Physics*, 56(2), 221-225.

481 Li, H., Tao, Q., Li, N., Tang, R., Zhao, Y., Zhu, H., Zhu, P., and Wang, X. (2016)
482 Pressure-induced structural transition of Y₂Zr₂O₇. *Journal of Alloys and
483 Compounds*, 660, 446-449.

484 Li, Q., Yang, J.-S., Huang, D.-H., Cao, Q.-L., and Wang, F.-H. (2014) Phase transition
485 and thermodynamic properties of ThO₂: Quasi-harmonic approximation
486 calculations and anharmonic effects. *Chinese Physics B*, 23(1), 017101.

487 Li, S., Ahuja, R., and Johansson, B. (2002) High pressure theoretical studies of actinide
488 oxides. *High Pressure Research*, 22, 471-474.

489 Macedo, P.M., Capps, W., and Wachtman Jr., J.B. (1964) Elastic constants of single
490 crystal ThO₂ at 25°C. *Journal of the American Ceramic Society*, 47(12), 651.

491 March, N.H., Richardson, D.D., and Tosi, M.P. (1980) Correlation of the superionic
492 transition temperature and Frenkel energy in fluorite crystals. *Solid State
493 Communications*, 35, 903-905.

494 Matveev, L.V., and Veshchunov, M.S. (1997) High-temperature transition of uranium
495 dioxide to the super-ionic state. *Journal of Experimental and Theoretical Physics*,
496 84(2), 322-329.

497 McDonough, W.F., and Sun, S.-s. (1995) The composition of the Earth. *Chemical
498 Geology*, 120, 223-253.

499 Nishio-Hamane, D., Dekura, H., Seto, Y., and Yagi, T. (2015) Theoretical and
500 experimental evidence for the post-cotunnite phase transition in zirconia at high
501 pressure. *Physics and Chemistry of Minerals*, 42(5), 385-392.

502 Office of Nuclear Reactor Regulation. (2012) Standard Technical Specifications Babcock
503 and Wilcox Plants Vol. 1., Washington, D.C.

504 Olsen, J.S., Gerward, L., Kanchana, V., and Vaitheeswaran, G. (2004) The bulk modulus
505 of ThO₂—an experimental and theoretical study. *Journal of Alloys and*
506 *Compounds*, 381(1-2), 37-40.

507 Perry, S.N., Pigott, J.S., and Panero, W.R. (2017) Ab initio calculations of uranium and
508 thorium storage in CaSiO₃-perovskite in the Earth's lower mantle. *American*
509 *Mineralogist*, 102(2), 321-326.

510 Prakapenka, V.B., Kubo, A., Kuznetsov, A., Laskin, A., Shkurikhin, O., Dera, P., Rivers,
511 M.L., and Sutton, S.R. (2008) Advanced flat top laser heating system for high
512 pressure research at GSECARS: application to the melting behavior of
513 germanium. *High Pressure Research*, 28(3), 225-235.

514 Prescher, C., and Prakapenka, V.B. (2015) DIOPTAS: A program for reduction of two-
515 dimensional X-ray diffraction data and data exploration. *High Pressure Research*,
516 35(3), 223-230.

517 Rittman, D.R., Turner, K.M., Park, S., Fuentes, A.F., Yan, J., Ewing, R.C., and Mao,
518 W.L. (2017) High-pressure behavior of A₂B₂O₇ pyrochlore (A=Eu, Dy; B=Ti,
519 Zr). *Journal of Applied Physics*, 121(4), 045902.

520 Rodriguez-Carvajal, J. (1993) Recent advances in magnetic structure determination by
521 neutron powder diffraction + FULLProf. *Physica B: Condensed Matter*, 192(55-
522 56).

523 Ross, M., Mao, H.K., Bell, P.M., and Xu, J.A. (1986) The equation of state of dense
524 argon: A comparison of shock and static studies. *The Journal of Chemical*
525 *Physics*, 85(2), 1028-1033.

526 Sevik, C., and Çağın, T. (2009) Mechanical and electronic properties of CeO₂, ThO₂,
527 and (Ce,Th)O₂ alloys. *Physical Review B*, 80(1), 014108.

528 Shein, I.R., Shein, K.I., and Ivanovskii, A.L. (2007) Elastic and electronic properties and
529 stability of SrThO₃, SrZrO₃ and ThO₂ from first principles. *Journal of Nuclear*
530 *Materials*, 361(1), 69-77.

531 Song, H.X., Geng, H.Y., and Wu, Q. (2012) Pressure-induced group-subgroup phase
532 transitions and post-cotunnite phases in actinide dioxides. *Physical Review B*,
533 85(6), 064110.

534 Toby, B.H., and Von Dreele, R.B. (2013) GSAS-II: The genesis of a modern open-source
535 all purpose crystallography software. *Journal of Applied Crystallography*, 46(544-
536 549).
537 Wang, B.-T., Shi, H., Li, W.-D., and Zhang, P. (2010) First-principles study of ground-
538 state properties and high pressure behavior of ThO₂. *Journal of Nuclear*
539 *Materials*, 399(2-3), 181-188.
540 Zhang, F.X., Lang, M., Liu, Z., and Ewing, R.C. (2010) Pressure-induced disordering and
541 anomalous lattice expansion in La₂Zr₂O₇ pyrochlore. *Phys Rev Lett*, 105(1),
542 015503.

543
544

545 **FIGURE CAPTIONS**

546 **Figure 1. a)** The fluorite crystal structure. **b)** The cotunnite-type crystal structure. Green
547 spheres represent the Th⁴⁺ cations, red spheres represent the O²⁻ anions.

548 **Figure 2.** Raw diffraction images and integrated diffraction patterns for three *in situ*
549 XRD measurements of sample B25. KBr was the pressure-transmitting medium, thermal
550 insulator, and pressure standard for the experiment. Pt acted as the laser-absorber for the
551 laser heating experiments.

552 **Figure 3.** Room temperature *P-V* data for thorianite from this study and the available
553 literature. The *ab initio* curve from Olsen et al. (2004) was developed using the
554 Generalized Gradient Approximation. The difference between the pressures predicted
555 from calculations and the measured pressure is shown in the bottom panel. The solid line
556 corresponds to the offset in ambient pressure volumes (predicted-measured). A
557 discontinuity is apparent in the data beginning around 15 GPa.

558 **Figure 4.** Raman spectra of ThO₂ collected at room temperature on increasing pressure.
559 Lines indicate the trajectories of peaks with increasing pressure. Colors are coordinated
560 with frequencies plotted in Fig. 5.

561 **Figure 5.** Raman vibrational frequencies as a function of pressure. Thorianite exhibits a
562 single vibrational mode (black triangles), whereas 8 separate peaks were identified for the
563 cotunnite-type phase. Upward solid triangles were measured on increasing pressure,
564 downward open triangles are decreasing pressure. Pressure dependencies were fit to
565 linear trends, which are shown in their corresponding color.

566 **Figure 6.** Phase diagram for ThO₂. Circles indicate in situ XRD measurements. Black:
567 thorianite; green: mixed phase; blue: cotunnite-type ThO₂. Orange X's: low density
568 thorianite determined from Fig. 3 (indicates anion sub-lattice disorder). Triangles indicate
569 relevant Raman measurements. Black: last spectrum with only thorianite; orange: some
570 new vibrational modes observed; green: all high-P modes are present; blue: phase
571 transformation appears complete. The grey shaded region indicates our preferred phase
572 boundary. See text for discussion.

573 **Figure 7.** Measured *P-V-T* data for thorianite and cotunnite-type ThO₂. Curves are
574 isotherms calculated using the equation of state parameters from Table 1. Isotherms are
575 color-coded by temperature. Residuals to the fits are provided in the bottom panels.

576 **Figure 8.** Individual lattice parameters and their ratios for cotunnite-type ThO₂. Black
577 lines are linear fits to the data. No temperature dependence was resolved for the lattice
578 parameter ratios.

579 **TABLES**

580 **Table 1.** Measured and calculated equation of state parameters for the polymorphs of
581 ThO₂. Bold values were held fixed in the fitting procedure. LH = laser-heated; RT =
582 room temperature; FP = full potential; PAW = projector-augmented wave method; PBE =
583 Perdew-Burke-Ernzerhof functional; LCGTO-FF = linear combinations of Gaussian type
584 orbitals-fitting function; LMTO = linear muffin-tin orbital method; LDA = local density
585 approximation; GGA = general gradient approximation; ASA = atomic-sphere
586 approximation; INS = inelastic neutron scattering. This table was adapted from Olsen et
587 al. 2004.

| Thorianite | | | | | |
|-------------------------------|-------------|----------|-------------------------|----------------------------|--------------|
| V_0 (cm ³ /mole) | K_0 (GPa) | K'_0 | αK_T (GPa/K) | Ref. | Method |
| 26.379(7) | 204(2) | 4 | 0.0035(3) | This study | LH-DAC |
| 26.44 | 198(2) | 4.6(3) | | Idiri et al. (2004) | RT-DAC |
| 26.37 | 262(4) | 6.7(5) | | Dancausse et al. (1990) | RT-DAC |
| 26.39 | 195(2) | 5.4(2) | | Olsen et al. (2004) | RT-DAC |
| 25.36 | 225 | 4.2 | | Olsen et al. (2004) | FP-LMTO-LDA |
| 26.60 | 198 | 4.2 | | Olsen et al. (2004) | FP-LMTO-GGA |
| 26.68 | 189 | 4.10 | | Perry et al. (2017) | GGA-PAW |
| 26.8 | 191 | 4.5 | | Wang et al. (2010) | GGA-PAW |
| 26.33 | 187.6 | 4.19 | | Li et al. (2014) | GGA-PBE |
| 26.77 | 184.5 | 4.49 | | Boettger (2009) | GGA-LCGTO-FF |
| 25.32 | 225 | 4.4 | | Kanchana et al. (2006) | FP-LMTO-LDA |

| | | | | | |
|---------------------------------------|--------|----------|-----------|---------------------------|--------------------|
| 26.58 | 198 | 4.5 | | Kanchana et al. (2006) | FP-LMTO-GGA |
| 26.16 | 198 | 4.91 | | Boudjemline et al. (2011) | GGA |
| 25.53 | 290 | | | Kelly and Brooks (1987) | LMTO-ASA |
| 26.76 | 192.8 | | | Shein et al. (2007) | FLAPW |
| 26.44 | 216 | | | Sevik and Çağın (2009) | LDA+U |
| | 175 | | | Harding et al. (1994) | Dirac-Fock approx. |
| | 221 | | | Li et al. (2002) | FP-LMTO-GGA |
| | 223 | | | Clausen et al. (1987) | INS |
| | 193(2) | | | Macedo et al. (1964) | Ultrasound |
| Cotunnite-type ThO₂ | | | | | |
| 24.75(6) | 190(3) | 4 | 0.0037(4) | This study | LH-DAC |
| 25.07 | 177 | 4.2 | | Perry et al. (2017) | GGA-PAW |
| 25.1 | 148 | 7.8 | | Wang et al. (2010) | GGA-PAW |
| 24.1 | 202.1 | 4.22 | | Li et al. (2014) | GGA-PBE |
| 24.7 | 206.8 | 4.94 | | Boettger (2009) | GGA-LCGTO-FF |
| 24.55 | 163.2 | 6.19 | | Boudjemline et al. (2011) | GGA |

588

589

590 **Table 2.** Pressure dependences of the measured Raman modes for thorianite and
 591 cotunnite-type ThO₂. ν_0 is the zero-pressure frequency. γ_i are the mode Grüneisen
 592 parameters for each vibrational mode, defined as $K_0(d\ln\nu_i/dP)$.

| Raman mode | ν_0 (cm⁻¹) | $d\nu_i/dP$ (cm⁻¹/GPa) | γ_i |
|-----------------------|---|---|------------------------------|
| F_{2g} | 460(2) | 2.37(9) | 0.96(4) |
| M1 | 497(3) | 1.55(6) | 0.51(2) |
| M2 | 577(3) | 2.04(8) | 0.59(2) |
| M3 | 294(3) | 1.28(7) | 0.69(4) |
| M4 | 325(4) | 1.05(8) | 0.54(4) |
| M5 | 365(3) | 0.83(6) | 0.39(3) |
| M6 | 465(3) | 0.85(7) | 0.32(3) |
| M7 | 497(3) | 1.55(6) | 0.41(4) |

593

594 **Table 3.** Linear fits to the lattice parameter ratios as a function of pressure for cotunnite-
595 type ThO₂.

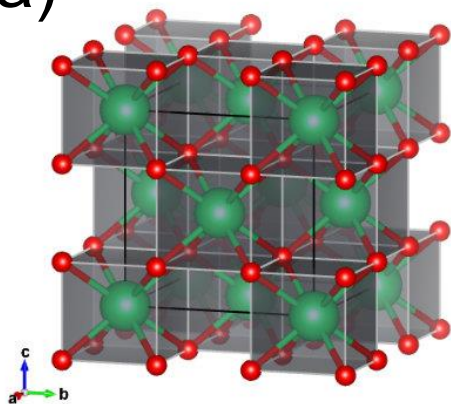
| Ratio | Slope (GPa⁻¹) | Zero-pressure value |
|--------------|---------------------------------|----------------------------|
| c/a | 0.00081(2) | 1.1391(9) |
| b/a | 0.00048(2) | 0.5962(8) |
| c/b | -0.00015(3) | 1.910(1) |

596

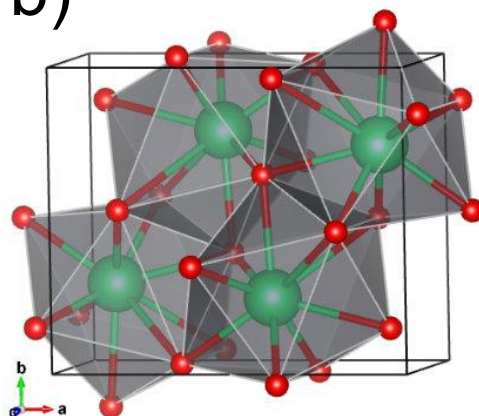
597

598 Fig. 1.

a)

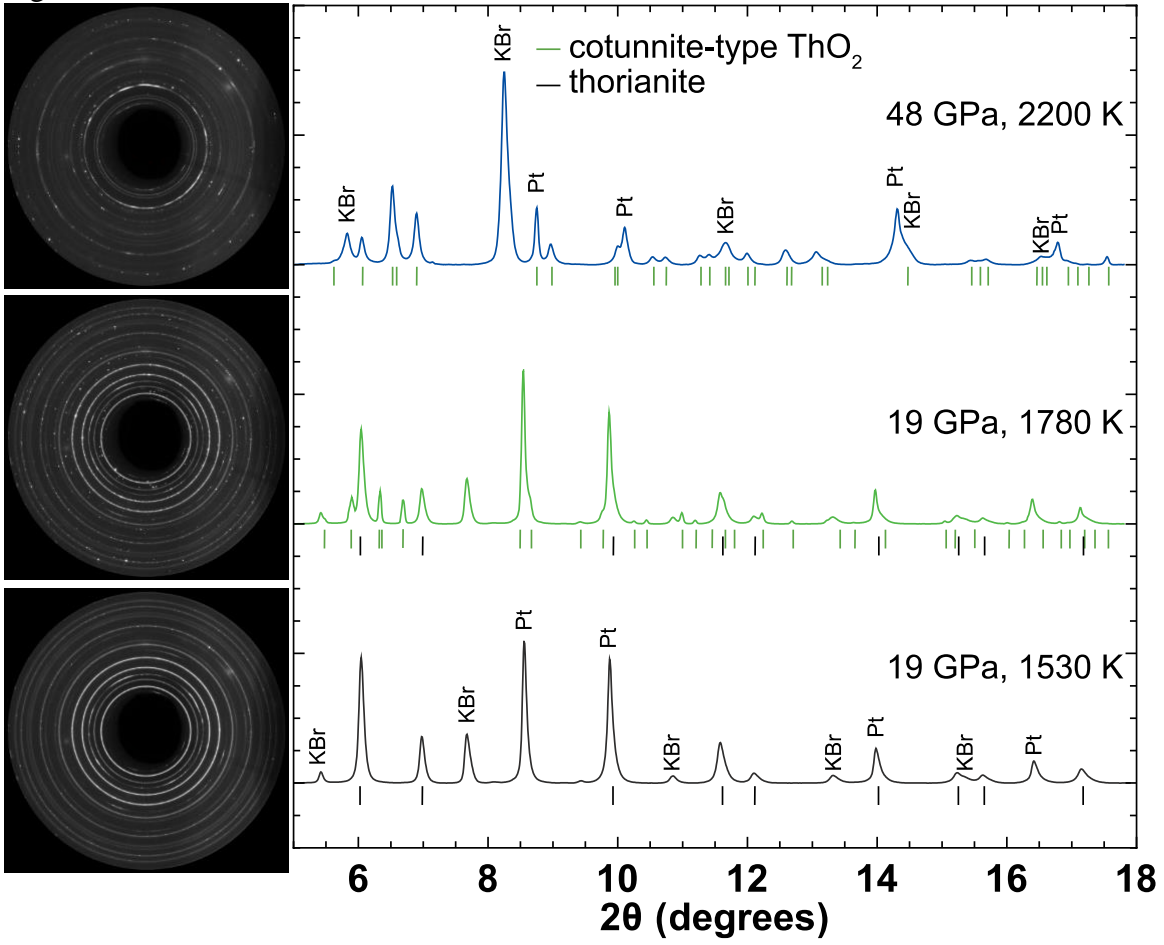


b)



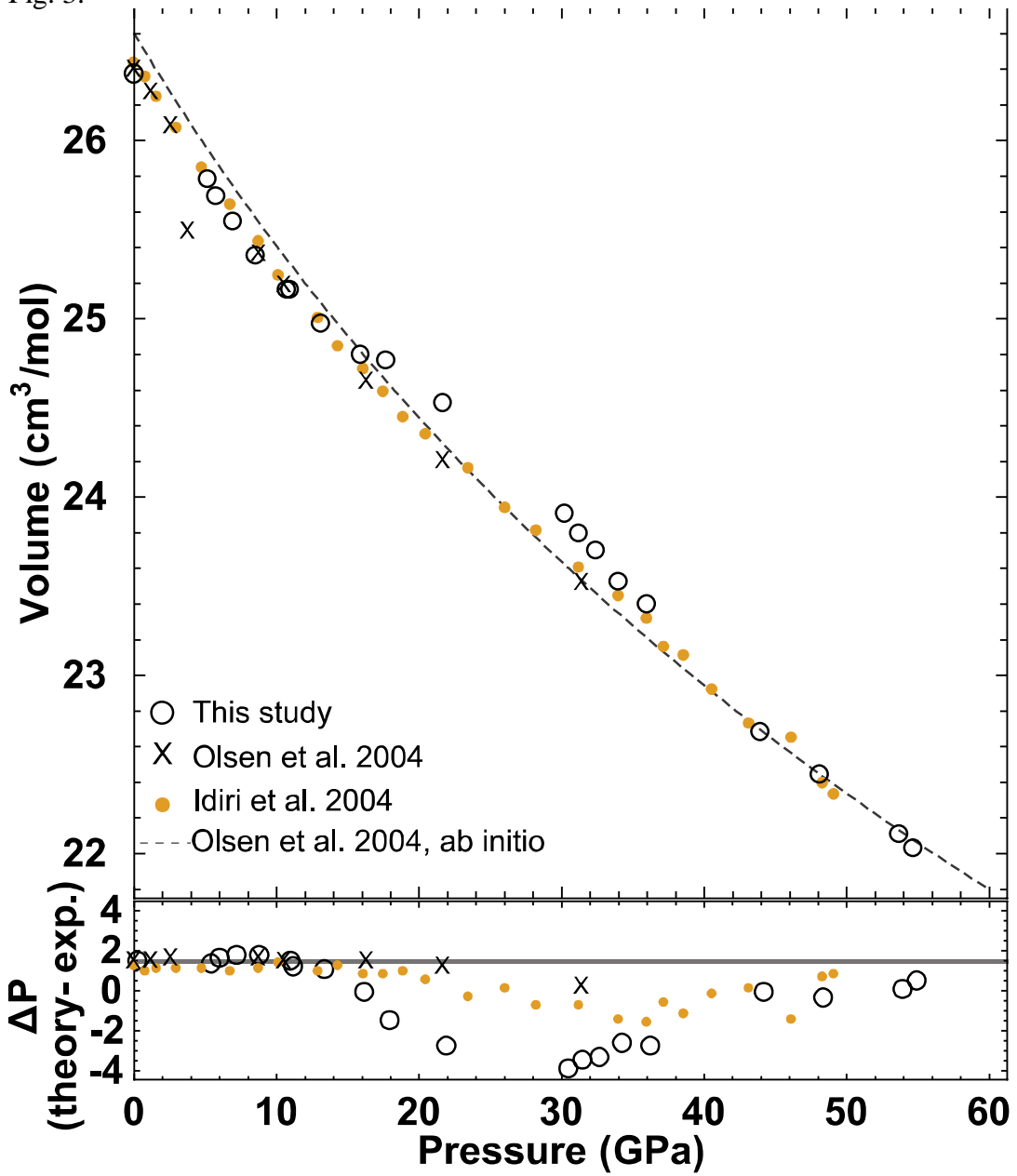
599
600

601 Fig. 2.



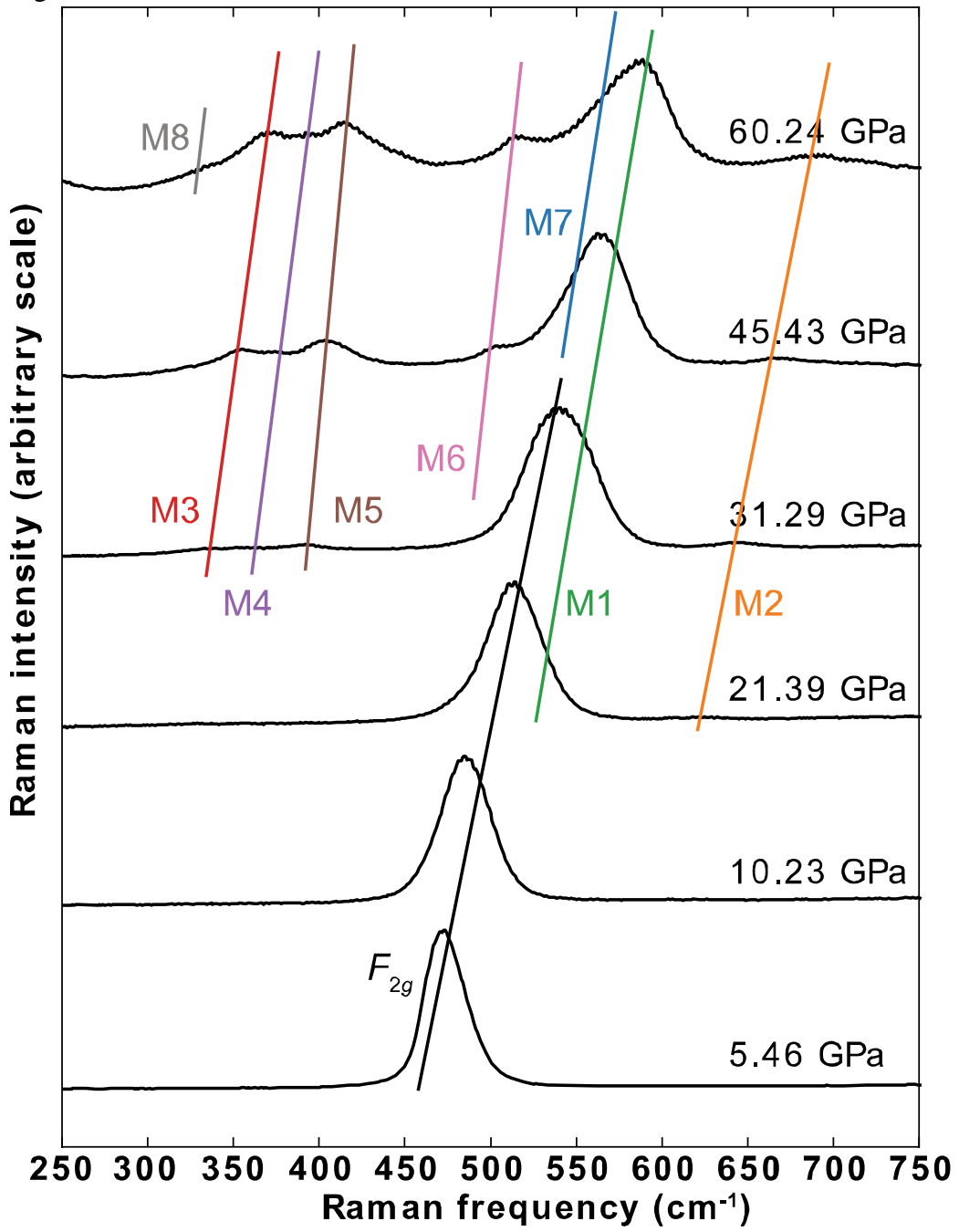
602
603

604 Fig. 3.



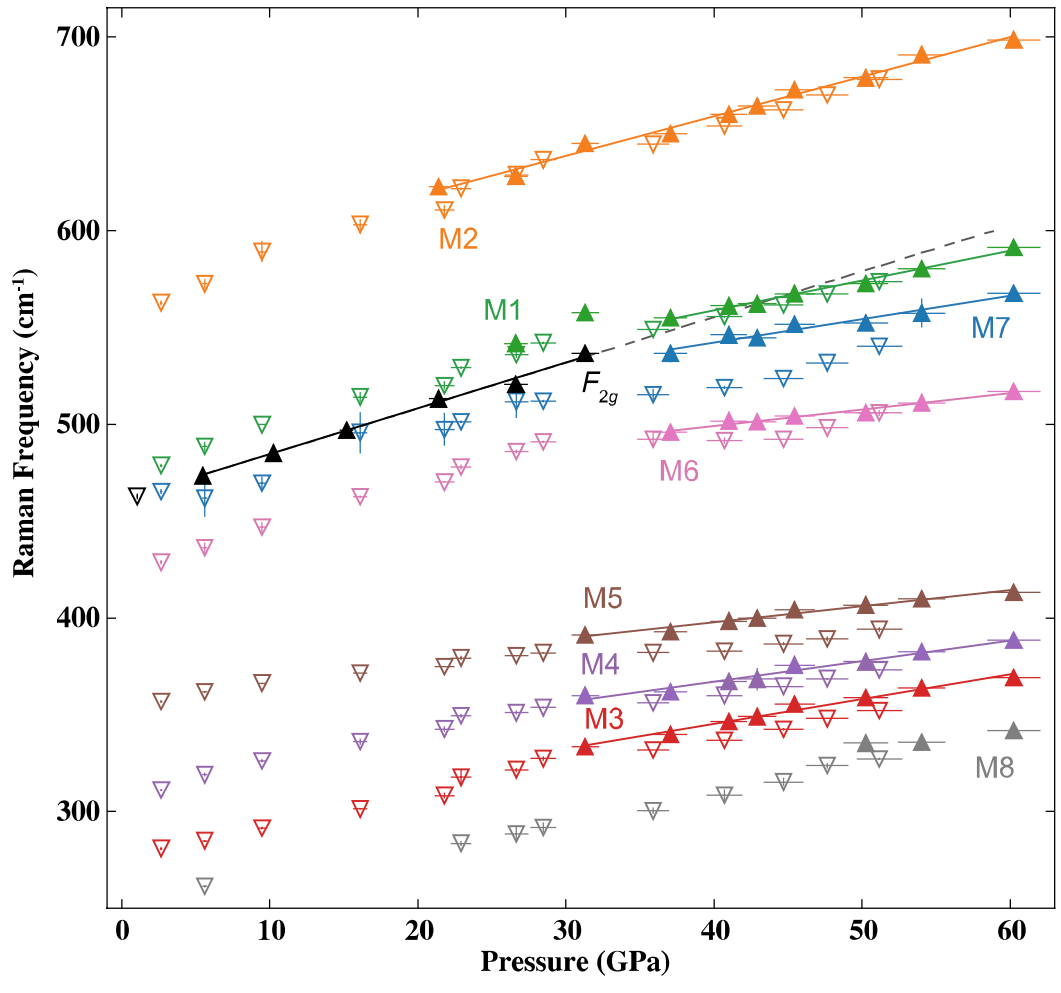
605
606

607 Fig. 4.



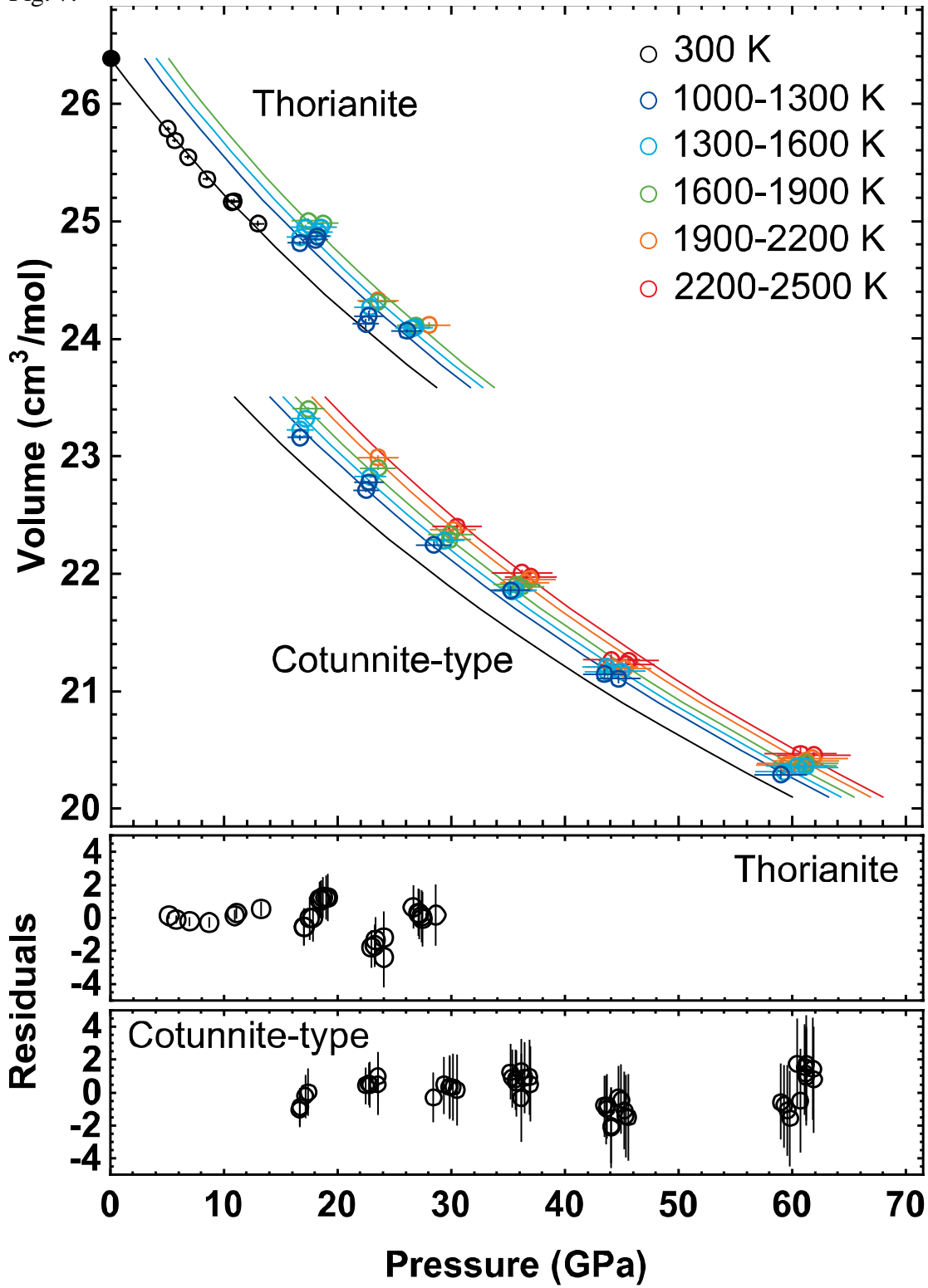
608
609

610 Fig. 5.



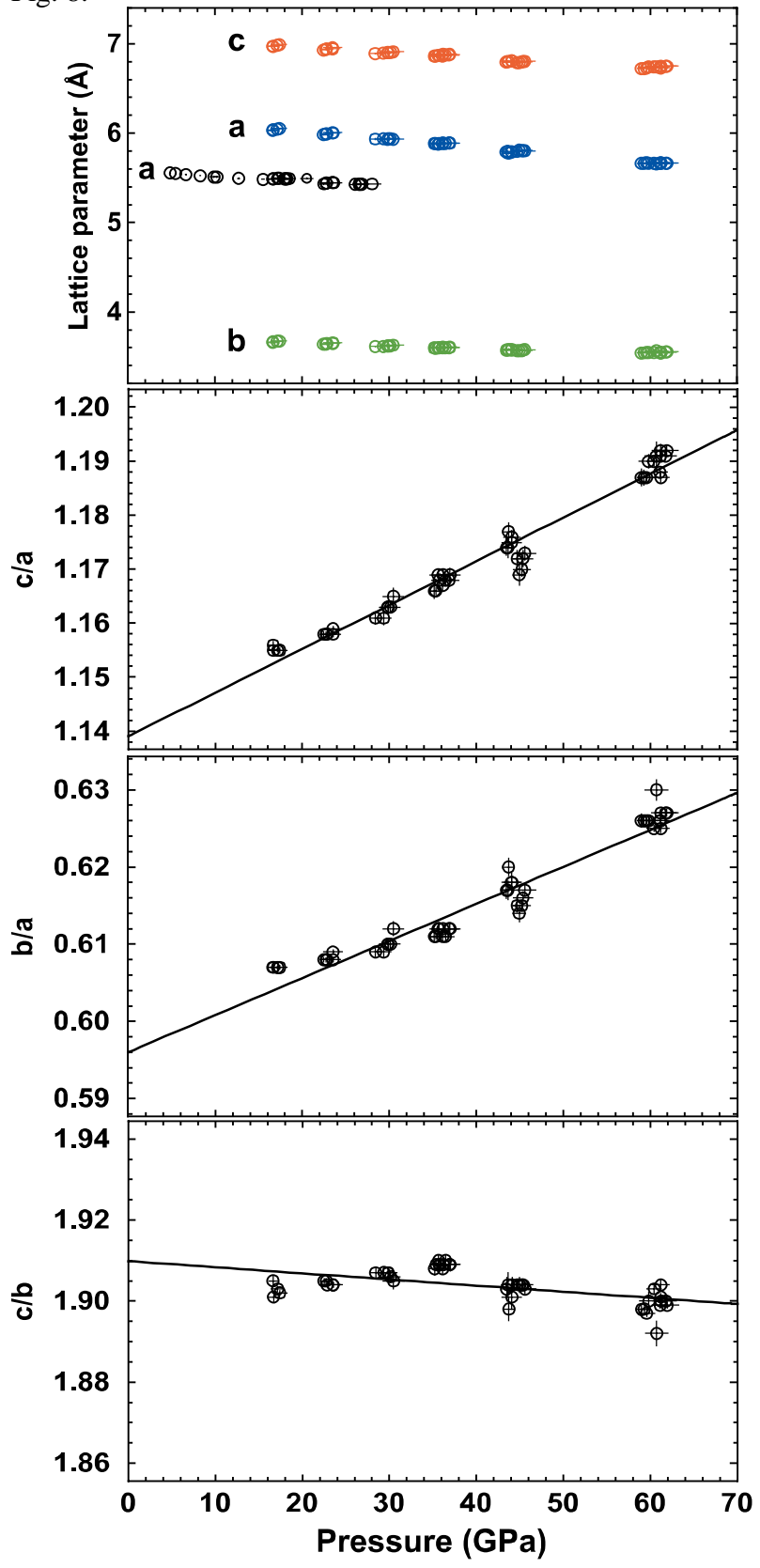
611
612

616 Fig. 7.



617
618

619 Fig. 8.



620